Defect engineering toward strong photocatalysis of Nb-doped anatase TiO$_2$: Computational predictions and experimental verifications

Sovann Khan [a,b], Haneol Cho [b,c], Donghun Kim [c], Sang Soo Han [c], Kyu Hwan Lee [b,d], So-Hye Cho [a,b,**], Taeseup Song [e,***], Heechae Choi [c,f,*]

[a] Materials Architecturing Research Center, Korea Institute of Science and Technology (KIST), Hwarangno 14-gil 5, Seongbuk-gu, Seoul 02792, Republic of Korea
[b] Department of Nanomaterial Science and Engineering, Korea University of Science and Technology, 217 Gajeong-ro, Yuseong-gu, Daejeon 34113, Republic of Korea
[c] Computational Science Research Center, Korea Institute of Science and Technology (KIST), Hwarangno 14-gil 5, Seongbuk-gu, Seoul 02792, Republic of Korea
[d] Small & Medium Enterprises Support Center, Korea Institute of Science and Technology (KIST), Hwarangno 14-gil 5, Seongbuk-gu, Seoul 02792, Republic of Korea
[e] School of Materials Science and Engineering, Yeungnam University, Gyeongsan 38541, Republic of Korea
[f] Center of Materials Simulation Research, Virtual Lab Inc., Hwarangno 14-gil 5, Seongbuk-gu, Seoul 02792, Republic of Korea

ARTICLE INFO

ABSTRACT

Understanding the roles of point defects in optical transitions is a key to the desirable engineering of photochemical materials. In this study, the origins of the significantly varying optical and photochemical properties of Nb-doped anatase TiO$_2$ were systematically investigated, using density functional theory (DFT) calculations and experimental verifications. We found from DFT calculations that the desirable band gap reduction of anatase TiO$_2$ by ∼0.1 eV reported in many of experimental reports and the resultant improvements of photocatalytic and photovoltaic efficiencies of Nb^{5+}-doped anatase TiO$_2$ are due to the formation of complex $(Nb_{Ti}-V_{Ti})^{3-}$ as the compensator of Nb_{Ti}^+. Our experiments demonstrated that the O$_2$-rich annealing, which is expected to increase the concentration of desirable $(Nb_{Ti}-V_{Ti})^{3-}$ complex, narrows band gap of TiO$_2$ and strongly enhances the photocatalytic activity of Nb-doped TiO$_2$ particle. On the contrary, pure TiO$_2$ showed rather worse photocatalytic performances when annealed in O$_2$-rich atmosphere, which is due to the formation of deep level by O-interstitial defect (O$_i$). Theoretically obtained charge effective masses could further explain the different photocatalytic activities of undoped and Nb-doped TiO$_2$.

© 2017 Elsevier B.V. All rights reserved.

1. Introduction

Anatase TiO$_2$ is regarded as the best photocatalytic material due to its abundance, low price, excellent chemical stability, and indirect band gap [1–3]. However, its wide band gap (∼3.20 eV) limits its uses only in ultraviolet range, and has driven enormous engineering efforts for higher efficiency [4–10].

Among the various methods of engineering anatase TiO$_2$ toward higher photocatalytic efficiencies, impurity doping is the most generally adopted strategy [2,8–12]. Band gap reduction (gaining more photons) by forming shallow impurity levels within the band gap are regarded as the best virtue of doping method since such shallow doping narrows band gap and makes the host crystal utilize more photons [10–14]. Nb^{5+}-doping is widely used to improve photocatalytic activities of anatase TiO$_2$ crystal. Many of experimental results demonstrated that doped Nb^{5+} improved electrical conductivity and tuned the band gap of anatase TiO$_2$ crystals [6,15–19], leading to highly increased photocurrents and photocatalytic activities.

Despite the long-reported excellent photocatalytic activities of Nb-doped anatase TiO$_2$ crystal, its practical use has been limited, due to the large and unexplained variations of its performances. For instances, the band gap of anatase TiO$_2$ was shown to be decreased

with increased doping concentrations, in the experiments of Das [20] and Yang [15], and their highest photocurrents were obtained by 0.1 at.% Nb doping in both works. On the other hand, Su's recent work showed that 2 at.% Nb doped TiO_2 sample makes highest photocurrent value and the band gap value fluctuate with doping concentration [16]. To be contradictory and interesting, Chandiran reported that Nb-doping rather opens up the band gap of host anatase TiO_2 wider (from 3.25 eV to 3.28 eV) [18]. In other works, the Nb-doping makes rather lower photoconductivity and photocatalysis of anatase TiO_2 crystal with unveiled reasons [17,19].

The origins of such great variations in optical and photochemical properties of Nb-doped anatase TiO_2 have never been clarified so far. Generally, large variations in optical and photochemical properties are mostly due to the formations of different phases or point defects. However, most of the experimental studies reported that Nb-doping concentration below 5 at.% does not induce secondary phases which is probably why the roles of point defects has not been tackled yet [21].

To make satisfactory quality control on the Nb^{5+}-doped TiO_2 as useful photocatalytic/photovoltaic material, exact understanding of atomic structures should be made since defects or dopant-defect complexes in concentration of ${\sim}10^{19}/cm^3$ can affect the optical properties and photochemical performances of entire crystals [22]. Since the oxidation number of Nb^{5+} is higher than that of Ti^{4+} of the host matrix, there is high possibility to accompany negatively charged (p-type) point defects apart from doped Nb^{5+} or nearby, to maintain the overall charge neutrality.

Many of recent first-principles and experimental studies showed that donor-doping makes dopant-dopant or dopant-defect complexes in the nearest sites [10,22,23]. Dominant defects or dopant-defect complexes evolve with the synthesis condition such as temperatures and types and partial pressures of treating gases. Two decades ago, an experimental work by Yang et al. showed that the Nb^{5+}-doping concentration above 0.4 at.% rather increased the length of space charge region (SCR) of anatase TiO_2 particle.[19] The increased SCR length with increasing doping concentration strongly suggests the existence of charge-compensating defects for Nb_{Ti}^+, such as V_{Ti}^{4-}, O_i^{2-}.

It is crucial to understand the atomic structures of doped oxides and their effects on the photochemical reactivity, to achieve reliable mass-production and fine engineering of the materials. At the same time, it is quite difficult to directly observe the atomic structures including point defects accompanied by introducing dopants – and to understand their contributions to the optical and photochemical properties of materials.

Here, we systematically investigate the roles of point defects in pure and Nb-doped anatase TiO_2 crystals in the optical transitions and photocatalytic activities using density functional theory (DFT) [24,25] calculations and experimental verifications. In the first half of this paper is devoted to the DFT calculations and thermodynamic modelling to explain the anomalous optical and photochemical phenomena of Nb-doped TiO_2 reported in the previous studies. In the second half, our experimental results and theoretical reasoning of various photocatalytic activities of Nb-doped TiO_2 synthesized in different conditions are represented. As expected from our DFT calculations, Nb-doped anatase TiO_2 nanoparticle annealed in the O_2 environment showed highly enhanced photocatalytic activity compared samples annealed in the N_2 or air environment. On the contrary, for the undoped anatase TiO_2 particle, O_2 annealing provided the lowest photocatalytic activity.

2. Calculation method

Density functional theory (DFT) calculations were performed using the generalized gradient approximation (GGA), with Perdew-
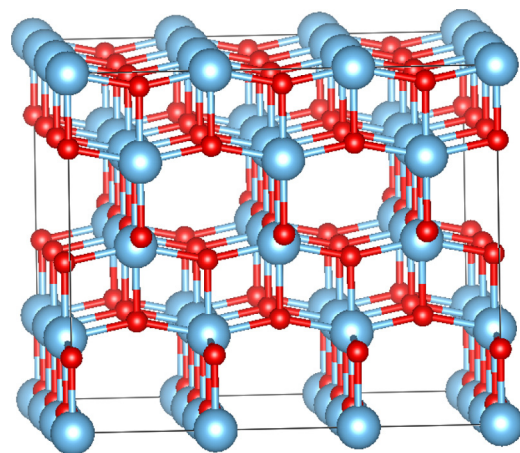

Fig. 1. $3 \times 3 \times 1$ anatase TiO_2 supercell with 36 Ti atoms and 72 O atoms. Red spheres are oxygen atoms, and blue spheres are titanium atoms. (For interpretation of the references to colour in this figure legend, the reader is referred to the web version of this article.)

Burke-Ernzerhof (PBE) parameterization [26,27]. We used the Vienna ab Initio simulation package (VASP) program [28]. Khon-Sham orbitals were expanded with a cutoff energy of 400.0 eV, and a $2 \times 2 \times 2$ and $4 \times 4 \times 4$ equally spaced k-point grids were employed for the Brillouin zone sampling in structural relaxations and electronic structure calculations, respectively [29]. A Hubbard U approximation term [30] was used to correct d-orbital splitting of the host Ti ions. Since Hubbard U, however, does not fully correct band gap, the transition point of the dopant or defect charges. We extrapolated transition point of dopant and defect charges from PBE to PBE + U to obtain the exact value inexpensively, using the following equation [31,32],

$$\varepsilon \left(q/q'\right) = \varepsilon \left(q/q'\right)^{PBE} + U + \frac{\Delta \varepsilon}{\Delta E} \left(E_g^{exp} - E_g^{PBE} + U\right) \qquad (1)$$

with

$$\frac{\Delta \varepsilon}{\Delta E} = \left(\frac{\varepsilon \left(q/q'\right)^{PBE+U} - \varepsilon \left(q/q'\right)^{PBE}}{E_g^{PBE+U} - E_g^{PBE}}\right), \qquad (2)$$

where $\varepsilon \left(q/q'\right)$ is the charge state transition point from charge q to q'. E_g^{exp}, $E_g^{PBE} + U$, and E_g^{PBE} are the band gaps of experiments, PBE + U, and PBE, respectively. The coefficient $\Delta \varepsilon / \Delta E_g$ is the rate of charge transition level change with respect to the change of band gap. The supercell of anatase TiO_2 was made up of $3 \times 3 \times 1$ of unit cell (108 atoms, Fig. 1), which is decided by careful convergence test of ours and previous theoretical work [10,33]. The cell volume and all atoms were fully relaxed. The Nb- and V- doped TiO_2 structures were modelled with the incorporation of one Nb or V ion at not only at Ti site but also defect-like sites, O- and interstitial sites. The typical problems of band gap underestimations were solved by using the hybrid functional methods (HSE) [34]. For our HSE06 calculations, a consistent screening parameter of $\mu = 0.2 \text{ Å}^{-1}$ was used for the semilocal exchange and the screened nonlocal exchange. We employed mixture of 22% of Hartree-Fock exchange with 78% of PBE exchange to obtain accurate band gaps of anatase TiO_2.

The formation energy of the anatase TiO_2 ($\Delta E_{TiO_2}^f$) was obtained using the equation,

$$\Delta E_{TiO_2}^f = E_{TiO_2} - E_{Ti} - E_{O_2}, \qquad (3)$$

where E_{TiO_2}, E_{Ti}, and E_{O_2} are the calculated total energies of the anatase TiO_2 crystal, solid Ti, and O_2 gas molecule, respectively. The calculated $\Delta E_{TiO_2}^f$ using PBE method is -9.08 eV/f.u., which is very close to the experimental value, -9.11 eV/f.u. Therefore, we
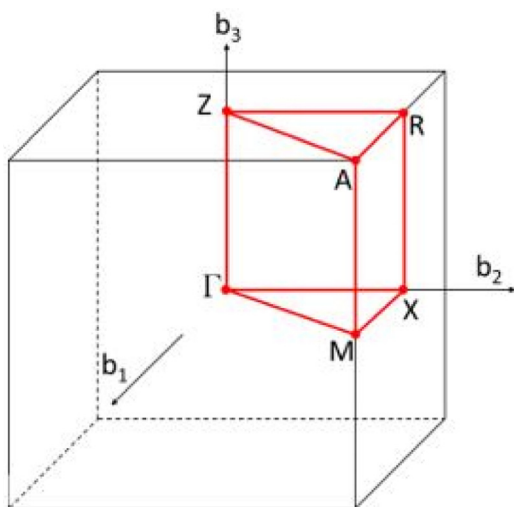
Fig. 2. First Brillouin zone of anatase TiO$_2$ (tetragonal crystal structure) with high-symmetry k-points.

regard that the point defect formation energies obtained from PBE calculations would be exact enough to predict the dominant point defects.

To calculate the formation energies of Nb-doping and point defects for varying temperature and pressure, the oxygen chemical potentials at a given temperature, T, and partial pressure, P, were expressed using the ideal gas approximation [35]:

$$\mu_O\left(T, P_{O_2}\right) = \frac{1}{2}\{\tilde{\mu}_{O_2}\left(T, P^{\circ}\right) + k_B T \ln(\frac{P_{O_2}}{P^{\circ}})\},\qquad(4)$$

where $\tilde{\mu}_{O_2}\left(T, P^{\circ}\right)$ is the O$_2$ and chemical potential at temperature T and standard pressure (P$^{\circ}$).

The chemical potential of O is given by:

$$\frac{1}{2}\Delta E^f_{TiO_2} < \mu_O \leq 0.\qquad(5)$$

Eq. (6) gives the doping energies with a charge q ($\Delta E^f(q)$), as a function of the Fermi level, using the equation [35]:

$$\Delta E^f(q) = E\left[D^q\right] \pm \mu_i - E^0 + q\left(E_v + \Delta V + \varepsilon_F\right),\qquad(6)$$

where $E\left[D^q\right]$ is the total energy of the TiO$_2$ supercell with dopants or/and defects in a charge q, E^{00} is the total energy of the defect-free TiO$_2$, μi is the chemical potential of the element i added to (removed from) the supercell to generate a point defect, Ev is the valence band maximum (VBM) of the defect-free TiO$_2$, ΔV is the shift in the VBM in the defective cell by a point defect, relative to that in the defect-free TiO$_2$, and εF is the Fermi level referenced to Ev.

We obtained theoretical band structures of pristine and doped/defective anatase TiO$_2$ supercell at high-symmetry k-points in the first Brillouin zone as depicted in Fig. 2 [36]. From the calculated band structures, we obtained theoretical effective masses of electron (m^*_e) and hole (m^*_h) carriers using the equations:

$$m^*_e = \hbar^2 \left(\frac{d^2 E(k)}{dk^2}\right)^{-1}\qquad(7)$$

$$m^*_h = -\hbar^2 \left(\frac{d^2 E(k)}{dk^2}\right)^{-1},\qquad(8)$$

where $\hbar$ and E(k) are the Planck constant and energy.

3. Experimental methods

3.1. Particles synthesis

TiO$_2$ and Nb-doped TiO$_2$ microspheres were synthesized by solvothermal synthesis as reported by Li et al. [37] 6 mM of titanium (IV) butoxide, Ti[O(CH$_2$)$_3$CH$_3$]$_4$, (Sigma-Aldrich Inc., USA) was dissolved into 50 mL non-aqueous mixture of solvents composed of 10 mL of acetylacetone, CH$_3$COCH$_2$COCH$_3$, (Kanto Chemical Co. Inc, Japan) and 40 mL of isopropyl alcohol, C$_3$H$_8$O, (Daejung Chemical, Korea). In case of Nb-doped sample, 0.06 mM of niobium n-butoxide, Nb[O(CH$_2$)$_3$CH$_3$]$_5$, (corresponding to 1 at.% of Ti) was also added into the mixing solvent. This solution precursor was mixed by a magnetic stirrer under an ambient condition for 2 h. The transparent mixture was poured into a 100 mL teflon-lined stainless-steel autoclave, and kept in a furnace at 200 °C for 4–12 h. After the reaction, white precipitate was formed and collected by centrifugation, and washed with ethanol for 3 times. Obtained product was dried in oven at 60 °C for 24 h and subsequently heated at 450 °C for 1 h in different gas environment (air, N$_2$ and O$_2$) at the flow rate of 2 lpm.

3.2. Characterizations

Properties of synthesized powder were analyzed by advanced characterizations. Particle morphologies were monitored by scanning electron microscopy (SEM) (Nova-SEM, FEI Company, USA); high-angle annular dark-field (HAADF) imaging, selected area electron diffraction (SAED) and energy-dispersive X-ray spectroscopy (EDS) elemental mapping were obtained by high-resolution-transmission electron microscopy (TEM/HR-TEM) (Talos F200X, FEI Company); crystal structure was studied by X-ray diffraction (XRD) (D8 Advanced, Brucker Corporation, USA); and UV/Vis absorption spectra were obtained by UV–vis spectrophotometer (Varian Cary 100, Agilent Technologies, USA). X-ray photoelectron spectroscopy data were obtained by PHI 5000 Versa Probe (Ulvac-PHI). Raman spectroscopy was performed with a Horiba Jobin-Yvon LabRam Aramis spectrometer with the 514.5 nm line of an Ar-ion laser as the excitation source.

Photocatalytic activities of TiO$_2$ samples were determined by methylene blue (MB) degradation under UV and visible light, respectively. 10 mg of TiO$_2$ powder was dispersed into 50 mL of MB (5×10^{-4} wt.%, Sigma Aldrich Inc., USA), and placed under visible light (Osram, HQI-TS/NDL, 150W (irradiation range = 370–800 nm without UV-cutoff filter)) for 5 h. After a predetermined time, irradiated MB solution was taken for centrifugation (13,500 rpm for 15 min) for the catalyst removal. Remained MB after photocatalytic degradation was determined by UV–vis absorption at $\lambda = 664$ nm, and calculated based on the calibration curve made with an MB reference solution.
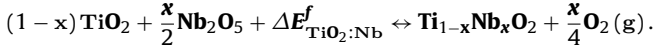
4. Results and discussions

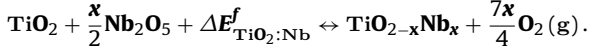### 4.1. Formation of pure and doped anatase TiO$_2$

The formation energies of Nb^{5+}-doping and point defects were calculated using Eq. (6) for the chemical reactions below (Reactions I–V). Temperature was set to the 700 K: combustion and annealing were performed at this temperature in many reported experiments [9,11] because above it, other polymorph phases, such as rutile or brookite are easily formed. Since our X-ray photoelectron spectroscopy (XPS) measurements suggested that niobium in all Nb-doped TiO$_2$ are Nb^{5+} species (see Fig. S1 in the Supporting information), solid niobium pentoxide (Nb$_2$O$_5$) was considered as reservoirs of the Nb^{5+}-dopant in our modelling. In addition, we con-

sidered not only the substitutions of Nb for Ti site, but also the defective substitution of Nb for O (Nb_O) and Nb-defect complex formations in various ways:
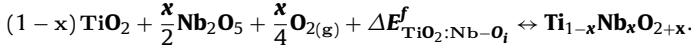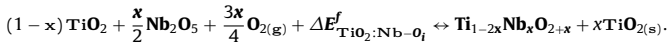
(I) Substitution of Nb for Ti (Nb_{Ti})

$$(1-x)\,TiO_2 + \frac{x}{2}Nb_2O_5 + \Delta E^f_{TiO_2:Nb} \leftrightarrow Ti_{1-x}Nb_xO_2 + \frac{x}{4}O_2\,(g).$$

(II) Substitution of Nb for O (Nb_O)

$$TiO_2 + \frac{x}{2}Nb_2O_5 + \Delta E^f_{TiO_2:Nb} \leftrightarrow TiO_{2-x}Nb_x + \frac{7x}{4}O_2\,(g).$$

(III) Forming complex of Nb_{Ti}-O_i

$$(1-x)\,TiO_2 + \frac{x}{2}Nb_2O_5 + \frac{x}{4}O_{2(g)} + \Delta E^f_{TiO_2:Nb-O_i} \leftrightarrow Ti_{1-x}Nb_xO_{2+x}.$$

(IV) Forming complex of Nb substitution for Ti and Ti-vacancy, Nb_{Ti}-V_{Ti}

$$(1-x)\,TiO_2 + \frac{x}{2}Nb_2O_5 + \frac{3x}{4}O_{2(g)} + \Delta E^f_{TiO_2:Nb-O_i} \leftrightarrow Ti_{1-2x}Nb_xO_{2+x} + xTiO_{2(s)}.$$

(V) Forming complex of Nb substitution for Ti and O-interstitial, Nb_{Ti}-O_{Ti}

$$(1-x)\,TiO_2 + \frac{x}{2}Nb_2O_5 + \frac{x}{4}O_{2(g)} + \Delta E^f_{TiO_2:Nb-O_i} \leftrightarrow Ti_{1-2x}Nb_xO_{2+x}.$$
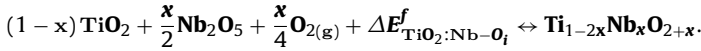
Kamisaka, et al., reported in their DFT study that the adjacent placement of Nb_{Ti} and V_O is energetically unfavourable [38]. Our test calculations also agree well with the results of Kamisaka [39] and hence, we excluded the Nb_{Ti}-V_O complex. In our calculations of $\Delta E_{Ti}O_2 : Nb^f$, the thermal energies of the solids (TiO_2:Nb, TiO_2, and Nb_2O_5) were ignored because their contributions to $\Delta E^f_{TiO_2:Nb}$ would be largely cancelled out. The calculated $\Delta E_{Ti}O_2 : Nb^f$ under O-rich, ambient, and O-poor conditions at temperature 700 K are presented in Fig. 3.

In O-rich (Fig. 3(a)) and ambient pressure conditions (Fig. 3(b)) at T = 700 K, Nb_{Ti}^+ is paired with the negatively charged $(Nb_{Ti}$-$V_{Ti})^{3-}$ complex. Then, considering the charge neutrality rule, the Nb^{5+}-doping in anatase TiO_2 matrices occurs with the reaction,

$$2Nb_2O_5 \leftrightarrow 3Nb_{Ti}^+ + (Nb_{Ti}\text{-}V_{Ti})^{3-}.$$
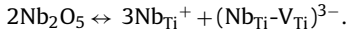
The formation energies of this reaction are pinned at negative value (-0.3 eV) in O-rich and ambient pressure conditions and the Fermi level is shifted from 0.6 eV (O-rich) to 1.0 eV (ambient), indicating that the doped Nb^{5+} can replace Ti^{4+} ion spontaneously. In an O-poor condition ($\Delta\mu_O = -3$ eV), only the neutral Nb_{Ti}^{00} appears with variable Fermi level between 2.8 and 3.2 eV (Fig. 3(c)) inferring no occurrence of charge-compensating defect. A number of experimental works reported that Nb^{5+} is stably doped in anatase TiO_2 since no other phases were detected at their doping level (typically, a few mole percent) [17–19,21]. The energetic stability of substitutional Nb-doping in anatase TiO_2, Nb_{Ti}^+ is found to come from the charge compensation by $(Nb_{Ti}$-$V_{Ti})^{3-}$.

On the other hand, the undoped anatase TiO_2 crystal is expected to accommodate two defects, Ti_i^{4+} and O_i^{2-}, in wide range of oxygen chemical potential. Therefore, undoped anatase TiO_2 is expected to possess high concentration of O_i^{2-} in O-rich conditions.

4.2. Electronic structures Nb-doped anatase TiO_2

Calculated electron density of states (DOS) of anatase TiO_2 crystals having O_i^{2-}, Nb_{Ti}^+, and $(Nb_{Ti}$-$V_{Ti})^{3-}$ are presented in Fig. 4. Interestingly, the Nb_{Ti}^+ does not reduce the band gap and this is opposite to the belief of many previous studies [15–19,20]. Rather, the conduction band (CB) is slightly shifted upward by Nb^{5+}-doping at Ti^{4+}-site. Chandiran et al.'s experiments showed exclusive band gap widening of anatase TiO_2 thin film by Nb-doping (3.25–3.28 eV) [18]. We argue that the band gap opening of anatase TiO_2 thin film

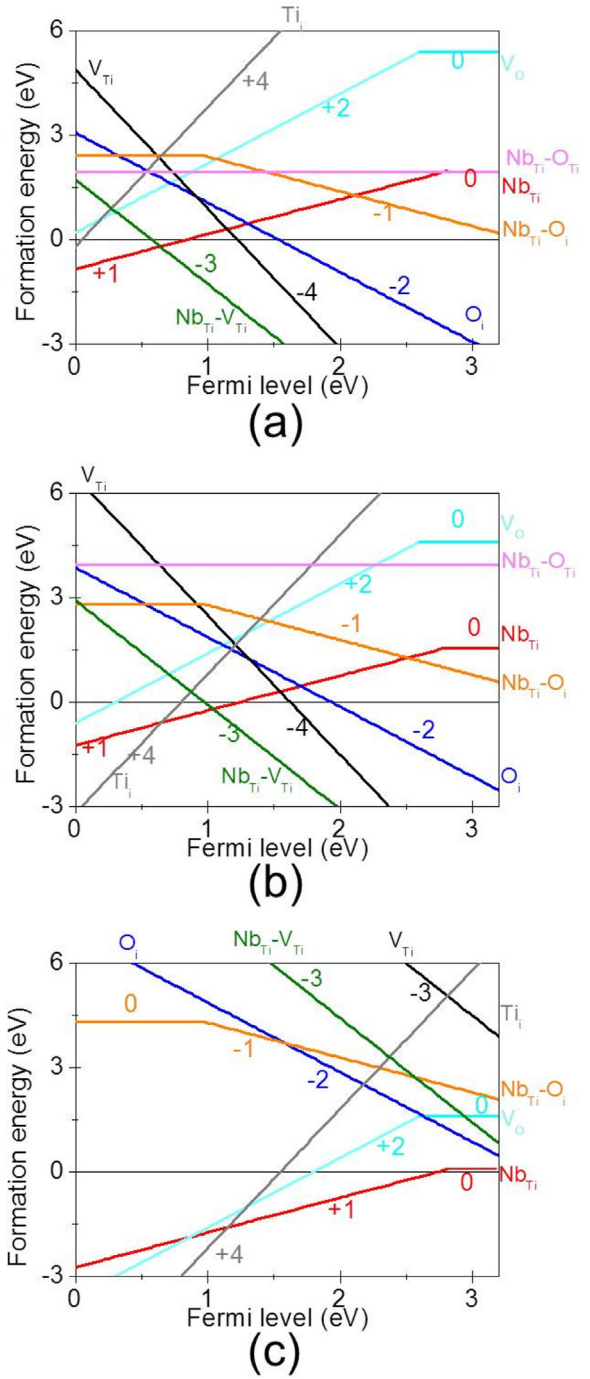

Fig. 3. Calculated formation energies of point defects and Nb-defect complexes in (a) O-rich limit, (b) ambient, (c) and O-poor ($\Delta\mu_O = -3$ eV) conditions.

in Chandiran's work [18] is due to the absence of charge compensating defect, $(Nb_{Ti}$-$V_{Ti})^{3-}$ as the result of controlled atmosphere. On the other hand, the defect O_i^{2-} induces a fully occupied deep level at 0.3 eV above valence band (VB). In addition, the CB edge was shifted downward significantly.

Band gap narrowing by Nb^{5+}-doping and defect formations was measured with the dopant or defect levels formed in density of states (DOS) calculations. We listed the band gap values of TiO_2 with Nb^{5+}-dopant and defects calculated by HSE06 methods in Table 1. As mentioned above, the band gap change by Nb^{5+}-doping was far less than the error range, 0.1 eV. The existence of only Nb_{Ti}^+ (without defects) rather slightly increases band gap of
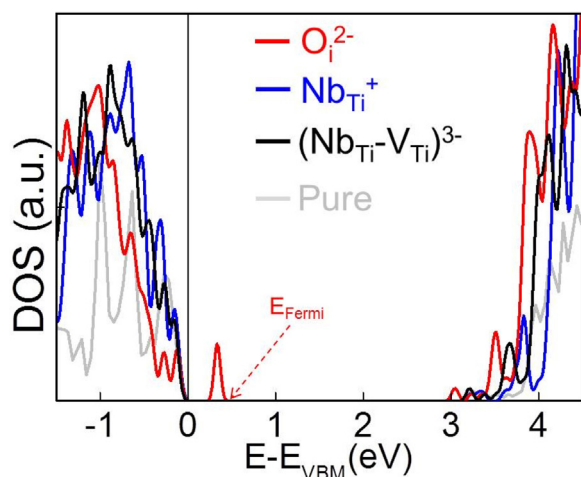
Fig. 4. Electron DOS of anatase TiO_2 supercells having three dominant defect and dopant-defect complexes from HSE06 calculation.

Table 1
Theoretical band gaps of TiO_2 having dominant defect and dopant-defect complexes obtained using HSE06 methods.

	Band gap (eV)	Impurity level
Pure	3.2	–
Nb_{Ti}^+	3.2	None
O_i^{2-}	2.7	Deep
$(Nb_{Ti}-V_{Ti})^{3-}$	3.1	Shallow

Table 2
Calculated effective mass ratios of electron and hole to real electron mass, $\left(\frac{m^*_e}{m_e}\right)$ and $\left(\frac{m^*_h}{m_e}\right)$ obtained from band edges of pure and defective TiO_2 in two important crystallographic directions, [101] and [001]. The effective masses of electron are estimated by fitting around Γ-point and those of holes are estimated around the maximum point of the valance band edge between Γ and M point.

	[101]		[001]	
	m_e	m_h	m_e	m_h
Pure	0.42	1.24	4.35	0.78
Nb_{Ti}^+	0.86	1.07	4.16	0.80
$(Nb_{Ti}-V_{Ti})^{3-}$	1.05	2.17	9.93	1.43
O_i^{2-}	0.99	1.47	7.98	1.06
Ti_i^{4+}	0.92	1.84	3.80	1.20

anatase TiO_2. Meanwhile, the O_i^{2-} formation is theoretically predicted to narrow the band gap of TiO_2 quite much, to 2.7 eV with deep and localized state above VBM. We think that the reduced band gap and rather degraded photocatalytic activity in previous experimental observations [18,20] are related with the formation of O_i^{2-} defect. Previous experimental work by Miyagi and co-workers reported that anatase TiO_2 film having deep levels showed significant electron-hole recombinations [39]. We attribute the fast charge recombination at deep level to the formation of O_i^{2-}.

As shown in Fig. 3, Nb_{Ti}^+ and $(Nb_{Ti}-V_{Ti})^{3-}$ are paired in ambient synthesis conditions, as the dominant n-type and p-type defects, respectively. Then, to accommodate desirable defect, $(Nb_{Ti}-V_{Ti})^{3-}$ complex in high concentrations, processing conditions must be O-rich. On the contrary, undoped anatase TiO_2 should avoid the formation of deteriorative defect, O_i^{2-}, which is expect to narrow band gap and degrade the photocatalytic activity due to the significant electron-hole recombination at its deep level.

Anatase phase of TiO_2 has an indirect band gap which is the reason why its carrier lifetime is longer than that of rutile phase (having a direct band gap).[5] It is quite necessary to check whether Nb-doping or defect formations alter the indirectness of anatase TiO_2 band gap and we obtained the band structures of TiO_2 having O_i^{2-}, Nb_{Ti}^+, and $(Nb_{Ti}-V_{Ti})^{3-}$ (Fig. 5). The calculated band structures show that the introduction of the defect or Nb^{5+} dopant in the anatase TiO_2 crystal does not change the indirectness of the band gap.

It has been reported from previous experimental works that the effective masses of charge carriers give important contributions to the photochemical reactivity of anatase TiO_2 crystals [5]. We obtained carrier effective masses from the computed band structures as summarized in Table 2. The ratio between the dominant facets of anatase TiO_2 crystals, (101) and (001), can be varied with syntheses conditions. In most cases, the (101) facet takes largest portions in anatase TiO_2 crystals. Our calculations show that the effective mass of hole is larger than that of electron in [101] direction for all of the doped and defective atomic structures considered

here. On the contrary, in [001] direction, the effective mass of hole is less than that of electron for all models. In the previous experimental observations, larger effective mass of hole was reported due to the dominance of (101) facet in normal conditions. Interestingly, only the Nb_{Ti}^+ reduces the hole effective mass, which indicates that the hole carrier transport can become faster with the introduction of Nb_{Ti}^+. In undoped anatase TiO_2, the dominant defects are Ti_i^{4+} and O_i^{2-} in ambient condition (Fig. 3). On the other hand, the dominant defects in Nb-doped TiO_2 are Nb_{Ti}^+ and $(Nb_{Ti}-V_{Ti})^{3-}$. Considering the average values of hole effective masses in the existences of the dominant defects in the [101] direction, 1.35 and 1.59, for Nb-doped and undoped TiO_2, respectively, Nb-doping can make an advantage of increasing hole transport efficiency.

When (001) surface of anatase TiO_2 becomes dominant, the electron carrier transport determines the photoreactivity of anatase TiO_2. Since the average effective mass of electron in [001] direction of Nb-doped and undoped TiO_2 is 5.60 and 6.59, in the existences of the dominant defects. Therefore, for either surface facet, Nb-doping can induce higher the carrier mobility compared to the dominant defect structures in undoped TiO_2.

To understand the charge distributions at the dominant charge-compensating point defects, $(Nb_{Ti}-V_{Ti})^{3-}$ and O_i^{2-}, we obtained the differential charge densities in the defective structures (Fig. 6). Interestingly, the triple negative charge of $(Nb_{Ti}-V_{Ti})^{3-}$ is highly delocalized at 2p-orbital of oxygen (Fig. 6(a)), while the charge of O_i^{2-} defect is localized at the interstitial oxygen and nearest lattice oxygen ion (Fig. 6(b)).

4.3. Structural and chemical properties of undoped and Nb-doped TiO_2 treated under different annealing conditions

In the previous session, our DFT calculation suggested that the high oxygen partial pressure during the formation of Nb-doped TiO_2 can enhance its photocatalytic activity while it adversely affects the photocatalytic activity of undoped TiO_2. To confirm the computational prediction for high photocatalytic activity of Nb-doped TiO_2 crystals formed in an oxygen rich condition, we synthesized undoped and Nb-doped anatase TiO_2 using a solvothermal method and heated them at 450 °C for 1 h in different gas environments (O_2, air and N_2). Both undoped and Nb-doped TiO_2 samples were found to be spherical with a large size distribution, 0.5–3 μm by the SEM analysis (Fig. 7(a)). The high magnification SEM images revealed that the spheres are composed of very fine particles of smaller than 30 nm in diameter (Fig. 7(b)) which is well in agreement with high resolution TEM and SAED analysis (see Fig. S2 in the supporting information, the SAED pattern showed a ring structure indicating the polycrystalline nature of the spheres). EDS mapping of Ti, O, and Nb elements for the Nb-doped TiO_2 showed Nb is evenly distributed in TiO_2 particles (no isolated Nb species such as Nb_2O_5 were found) (Fig. 7(c)).
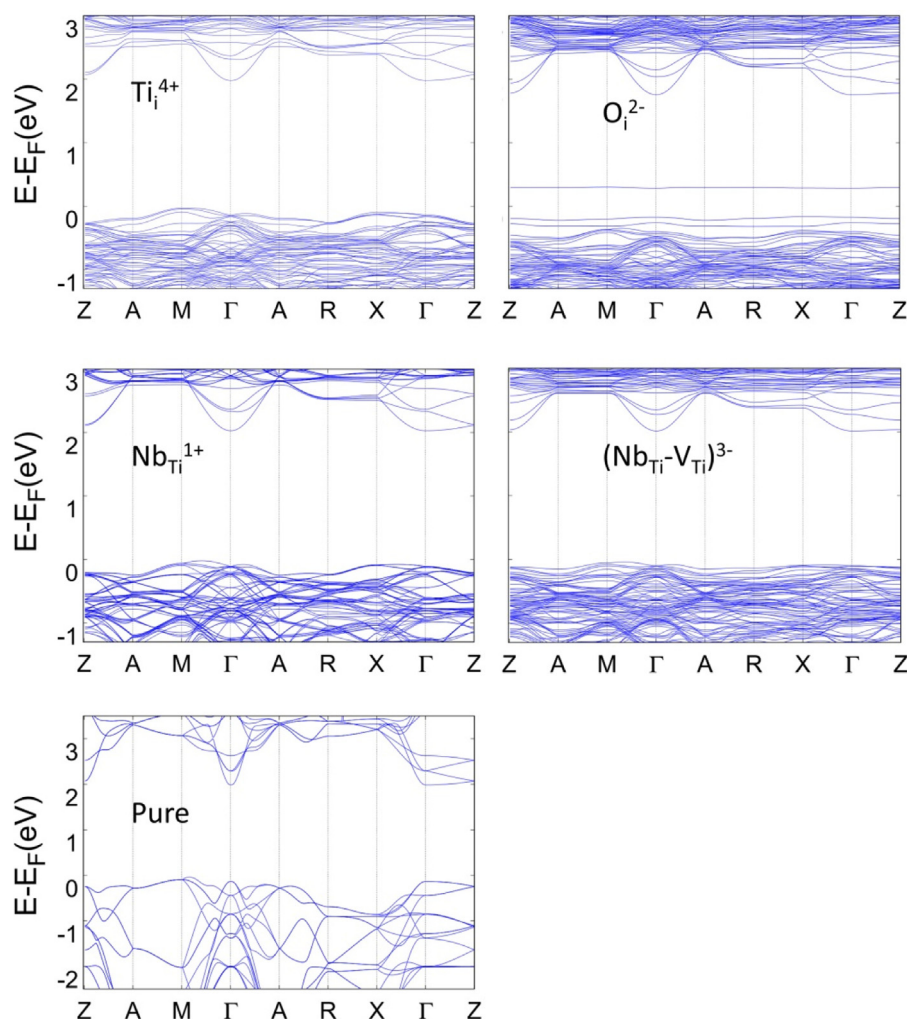
Fig. 5. Calculated band structures of pure and doped/defective anatase TiO$_2$ supercells.
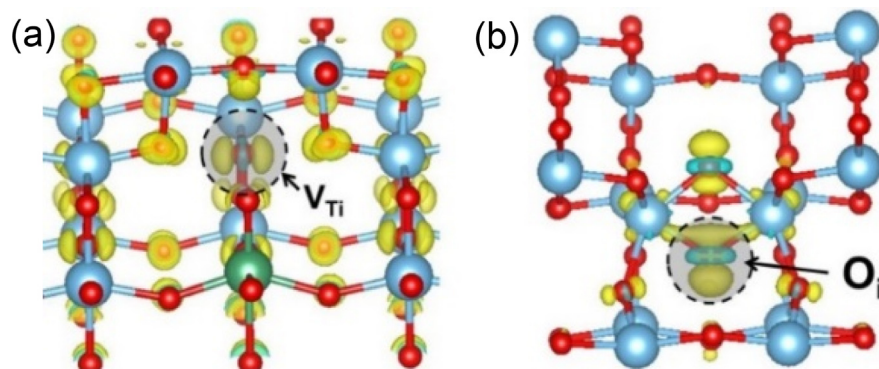

Fig. 6. Differential charge density of TiO$_2$ matrices having (a) a (Nb$_{Ti}$-V$_{Ti}$)$^{3-}$ complex and a (b) O$_i$$^{2-}$ defect. The charge of the former defect is highly delocalized over lattice oxygen ions, while the latter defect induces localized charge density at the site of defect and a neighbouring lattice oxygen ion. Light blue, green, and red spheres indicate Ti, Nb, and O atoms. (For interpretation of the references to colour in this figure legend, the reader is referred to the web version of this article.)

Based on long-scanned XRD data, both undoped and Nb-doped TiO$_2$ showed a pure anatase phase of TiO$_2$ (space group: $I41/amd$, $a = 3.7813$ Å, $c = 9.4806$ Å) according to JCPDS#21-1272, regardless of annealing condition (Fig. 8(a)). The broader peaks obtained from as-synthesized samples infer that as-synthesized samples have lower crystallinity [40]. High resolution XRD spectra of the (101) plane of anatase TiO$_2$ show that small shifts to lower angles occur with peaks of all Nb-doped TiO$_2$ in respect to peaks of undoped TiO$_2$

(Fig. 8(b)). Cell volumes calculated from the XRD spectra showed an increase by the introduction of Nb^{5+} doping (Table 3) which is due to the different ionic radius of Nb^{5+} and Ti^{4+} (the ionic radius of Nb^{5+} = 0.64 Å and that of Ti^{4+} = 0.61 Å) [41]. The increased cell volumes, therefore, confirm that Nb ions are doped into TiO$_2$ crystals.

Raman spectra obtained with the TiO$_2$ samples (Fig. 9(a)) showed major peaks at 144 cm^{-1} (E$_g$), 197 cm^{-1} (E$_g$), 396 cm^{-1} (B$_{1g}$), 513 cm^{-1} (A$_{1g}$), 519 cm^{-1} (B$_{1g}$) and 639 cm^{-1} (E$_g$) which are
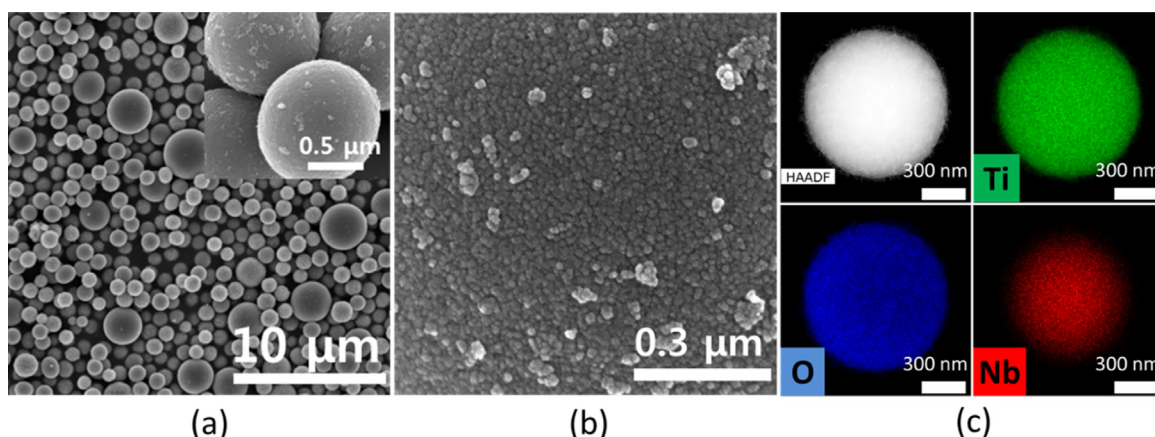
Fig. 7. As-synthesized Nb-doped TiO$_2$: (a) a SEM image at the magnification of 5,000x; (b) a SEM image at the magnification of 150,000x; (c) a HAADF image and EDS mapping images of Ti, Nb, and O (clockwise).
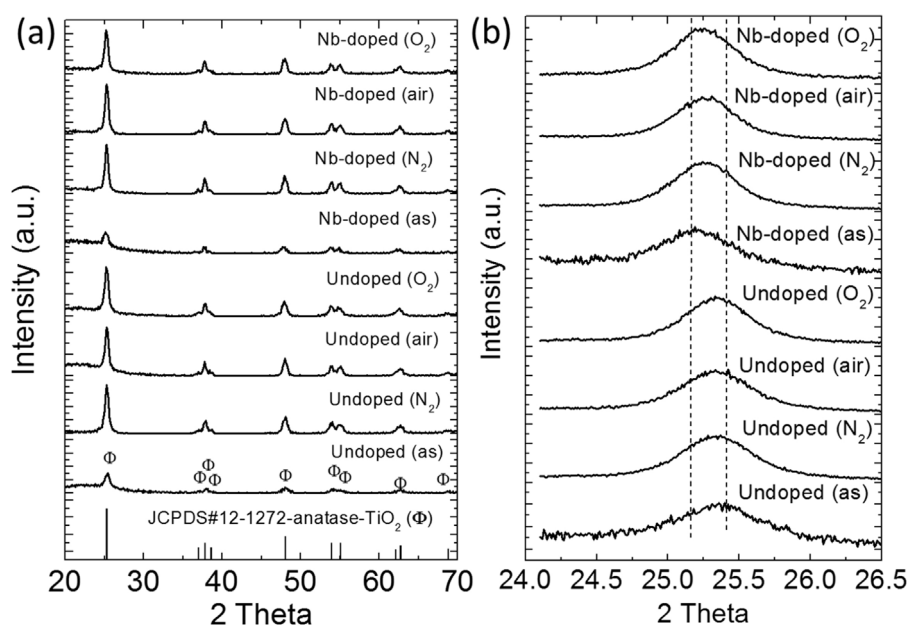

Fig. 8. XRD spectra of undoped and Nb-doped TiO$_2$, as-synthesized and annealed in different gas environment (N$_2$, air, and O$_2$) from bottom to top: (a) long-range XRD and (b) slow-scanned short range XRD spectra.

Table 3
Cell volumes obtained from XRD patterns (Fig. 8(b)) and elemental analysis calculated from XPS spectra (Figs. S1 and 10).

Samples	Cell volume (Å^3)	Elemental ana. XPS (%)	
		O $_{O-Ti}$	Nb/Ti
undoped-as	135.20	67.11	0
undoped-N$_2$	136.22	66.09	0
undoped-air	136.31	67.39	0
undoped-O$_2$	136.37	67.94	0
Nb-doped-as	137.61	67.19	1.68
Nb-doped-N$_2$	137.28	66.89	1.75
Nb-doped-air	137.26	66.94	1.76
Nb-doped-O$_2$	137.41	67.19	1.85

in good agreement with Raman bands of anatase TiO$_2$ [42]. Changes in the Raman spectra by Nb doping were observed with the main E$_g$ peak at 100–200 cm^{-1} as shown in Fig. 9(b). The peak shifted to higher wavenumbers with the Nb introduction which is an indicative of the expanded crystal lattice of TiO$_2$ by the effective Nb^{5+} doping [43].

Chemical compositions of all TiO$_2$ samples were carefully analysed by XPS (Fig. S1). Determined by binding energies of each elements in the long-range XPS spectra, the Nb-doped TiO$_2$ contains about 1.7 at.% of Nb in respect to Ti (Table 3). The XPS analysis of O 1s, Ti 2p, and Nb 3d core levels of all TiO$_2$ samples were obtained and shown in Fig. 10. The Ti 2p binding energies were observed at ∼458.7 eV (2p$_{3/2}$) and ∼464.5 eV (2p$_{1/2}$), distinctive for the Ti^{4+} ionic state, for all samples with little variation in the peak position. In addition, each peak was fitted well in a single peak, inferring that the oxidation state of Ti is quite stable regardless of reaction conditions. The major peak for O 1s binding energy was observed at ∼530 eV with two minor peaks at 531.3 eV and 532.2 eV. The major peak corresponds to the lattice oxygen (O$_{O-Ti}$) species in TiO$_2$ crystals and the minor peaks at 531.3 eV and 532.2 eV correspond to the surface hydroxyl oxygen (O$_{O-H}$) and the chemisorbed oxygen (O$_{O-O}$) species, respectively. The binding energies of Nb 3d were observed as two peaks at ∼207.3 eV and 209.9 eV, each of which was fitted well into a single peak corresponding to Nb 3d$_{5/2}$ and Nb 3d$_{3/2}$, respectively, of the oxidation state of Nb^{5+} [44]. The observation of Ti and Nb XPS peaks suggests that neither
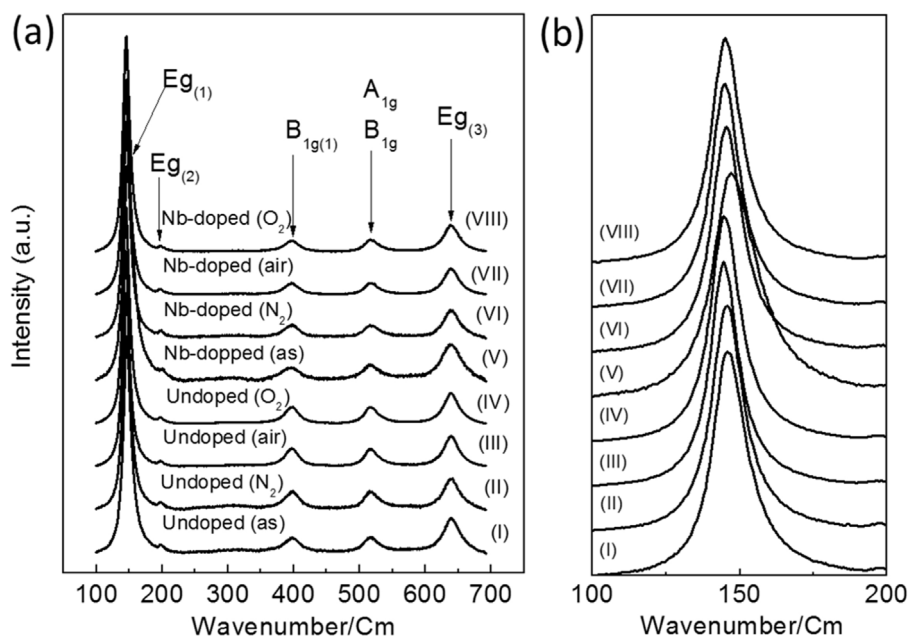
Fig. 9. Raman spectra of undoped and Nb-doped TiO_2: (a) long-range spectra and (b) magnified spectra at 100–200 cm^{-1}.
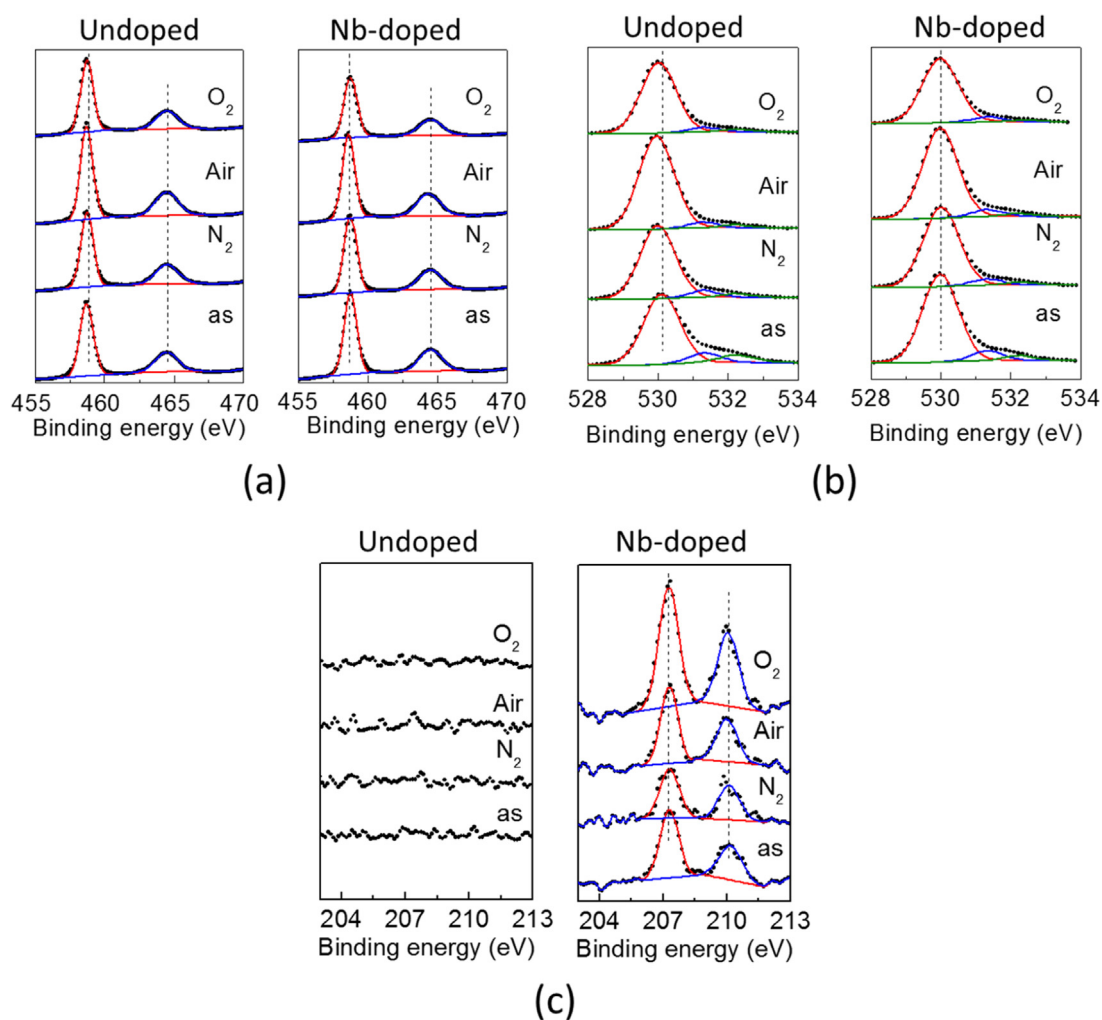

Fig. 10. XPS spectra of undoped and Nb-doped TiO_2 as-synthesized and annealed at different gas environments (N_2, air, and O_2): (a) Ti 2p peaks; (b) O1s peaks, and (c) Nb 3d peaks.
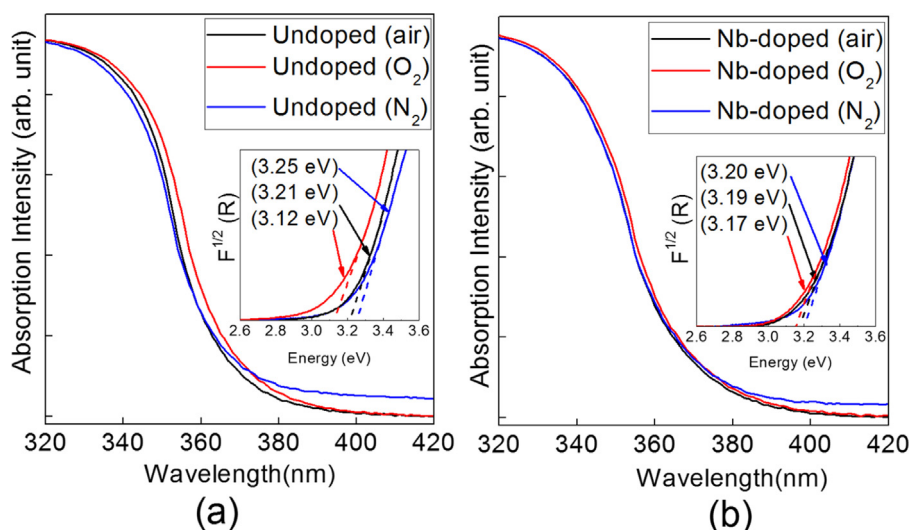
Fig. 11. Photoabsorption spectra of (a) undoped and (b) Nb-doped anatase TiO_2 annealed in N_2, air, and O_2 (the insets are plots of Kubelka-Munk function versus photon energy absorbed).

Nb doping nor annealing in different gas environments alters the oxidation states of Ti and Nb (they remain as Ti^{4+} and Nb^{5+}).

As suggested in the session **a** and **b**, the Nb doping in anatase TiO_2 stabilizes the formation of a defect pair, $(Nb_{Ti}-V_{Ti})^{3-}$, while the interstitial oxygen defect, O_i^{2-}, is preferentially formed in the undoped anatase TiO_2 in the O_2-rich condition. This notion was well supported by our XPS data. The quantification results of the lattice oxygen (O_{O-Ti}) species in percentage are provided in Table 3, showing that the contents of O_{O-Ti} in undoped TiO_2 gradually increased as the annealing gas environment was changed from N_2 to air and to O_2 (no such changes were found with Nb-doped samples). When Nb contents were compared to Ti contents, the Nb-doped TiO_2 annealed in O_2 environment provided higher ratio (Nb/Ti = 1.85) than the as-synthesized one (Nb/Ti = 1.68) supporting the possibility of $Nb_{Ti}-V_{Ti}$ formation (less contents of Ti).

4.4. Optical properties and photocatalytic activities of Nb-doped TiO_2 and undoped TiO_2 treated under different annealing conditions

The photoabsorptions of undoped and Nb-doped TiO_2 were measured to compare their band gaps by different annealing conditions (Fig. 11). As shown in the calculated electron DOS (Fig. 4),

the O_2-rich condition would lead to the reduced band gap of both undoped and Nb-doped anatase TiO_2 while the origins of each band gap reduction are different — O_i^{2-} for undoped TiO_2 and $(Nb_{Ti}-V_{Ti})^{3-}$ for Nb-doped TiO_2. This prediction matched well with our experimental measurement of optical band gaps by photoabsorption spectra of undoped and Nb-doped TiO_2 annealed in different gas environments. Albeit the Nb doping caused overall reduction of band gaps of TiO_2, the O_2-rich condition provided further reduction of band gaps for both undoped and Nb-doped TiO_2. However, the greater degree of a band-gap reduction was found with undoped TiO_2 (0.09 eV reduction for undoped TiO_2 from the air-annealed sample vs. 0.02 eV reduction for Nb-doped TiO_2, see the insets of Fig. 11). The band gaps for all samples are summarized in Table 4 and compared with the calculated values.

Next, the photocatalytic activities of undoped and Nb-doped TiO_2 samples were tested by MB degradation rates under the UV light illumination (Fig. 12). It is clearly seen that the highest activity of Nb-doped TiO_2 was found with the thermal treatment in O_2-rich condition (the black square in Fig. 12) while the lowest activity of undoped TiO_2 was made after O_2-rich annealing (the orange triangle). As suggested by our calculation, the O_i^{2-} defect may occur in undoped TiO_2 in the O_2-rich environment and form the localized deep level above VBM mediating electron-hole recombination.
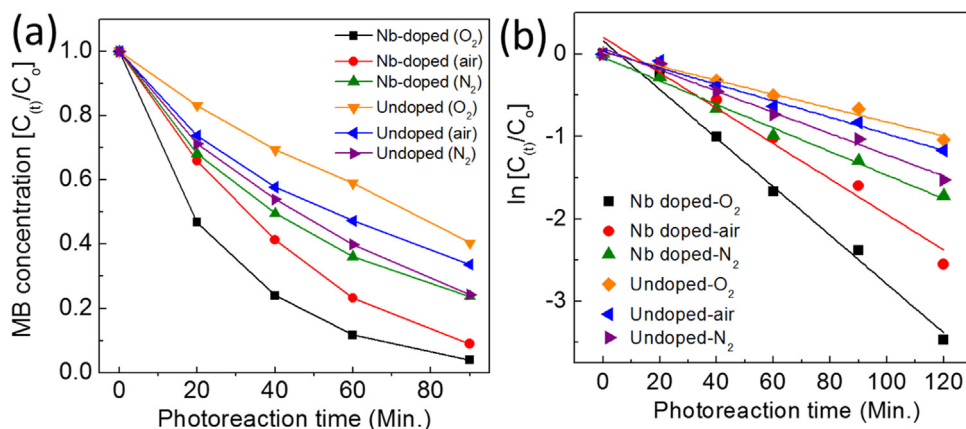

Fig. 12. Photocatalytic degradation of MB by undoped and Nb-doped TiO_2 as-synthesized and annealed in different gas environments (N_2, air, and O_2) under UV light: (a) relative concentration of MB (C_t/C_0) as a function of time; (b) plots of $\ln(C_t/C_0)$ as a function of time (C_t is MB concentration of a given time, t, and C_0 is the initial concentration of MB at time = 0). The slopes in Fig. 12(b) are decay constants of MB degradation.

Table 4
Optical band gaps measured by photoabsorption (Fig. 11) and calculated (Fig. 4) and the rate constants of MB degradation by undoped and Nb-doped TiO_2 annealed in different gas environments (N_2, air, and O_2) (Fig. 12).

Samples	Measured band gap (eV)	Calculated band gap (eV)	Rate constant, k (min^{-1})
undoped-N_2	3.25	3.2	0.0129
undoped-air	3.21	3.2	0.0100
undoped-O_2	3.12	2.7	0.0084
Nb-doped-N_2	3.2	3.2	0.0143
Nb-doped-air	3.19	3.2	0.0215
Nb-doped-O_2	3.17	3.1	0.0295
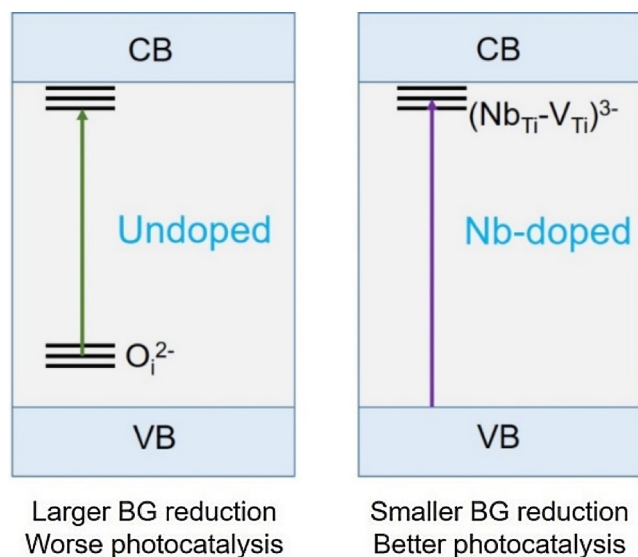
Scheme 1. Comparison of impacts of O-rich annealing on the defect levels of undoped and Nb-doped anatase TiO_2 nanocrystals.

On the other hand, the $(Nb_{Ti}-V_{Ti})^{3-}$ defect pair may form in Nb-doped TiO_2 and play the key role in narrowing the band gap of TiO_2 and enhancing photocatalytic activity with a shallow level. The rate constants of MB degradation by all samples are summarized in Table 4 and schematic comparison of impacts of O_2-rich annealing on the defect levels of undoped and Nb-doped TiO_2 is provided in Scheme 1.

It is worthy comparing the Nb-doped TiO_2 to the case of W-N codoped anatase TiO_2 system [10,12,13]. The W-N codoped TiO_2 has stronger photocatalytic activity when annealed in O-poor and N-rich conditions. Such annealing conditions were found via exhaustive experimental efforts [11–13] and the origins were clarified by our previous theoretical work [10]. A correct defect engineering direction can be efficiently achieved when defect equilibria and their effects on the electronic structures are firmly understood. Our approach, DFT thermodynamics modelling, to tune the optical properties and enhance the photocatalysis of Nb-doped TiO_2 crystal is an efficient way to guide thermal processing and is expected to be broadly used in a number of solar energy conversion applications.

5. Conclusions

Desirable defect engineering for Nb-doped TiO_2 photocatalyst, O_2-rich annealing, could be suggested from our systematic investigation on the defect equilibria of Nb^{5+}-doped anatase TiO_2 crystalline and their effects on the electronic structures, using DFT calculations. From our DFT calculations and thermodynamic modelling, Nb^{5+} ions at host Ti^{4+} site (Nb_{Ti}^{+}) were found to be charge-compensated by $(Nb_{Ti}-V_{Ti})^{3-}$ complex, as the dominant

defect at atmospheric and O-rich conditions. The $(Nb_{Ti}-V_{Ti})^{3-}$ defect complex is more stabilized in O-rich conditions and was predicted to improve the photocatalytic activity by forming shallow defect level. Undoped TiO_2 in O-rich conditions, on the contrary, was theoretically predicted to accommodate O_i^{2-} defect, which is expected to induce localized deep level and degrade photocatalysis of TiO_2 host. Our theoretical predictions were well demonstrated with our experiments: the photocatalytic activity of Nb^{5+}-doped TiO_2 crystals was significantly improved with O_2-rich annealing condition, which can be attributed to the increased concentration of $(Nb_{Ti}-V_{Ti})^{3-}$ defect complexes. Our combined DFT and experimental work demonstrates the necessity of charge-compensating $(Nb_{Ti}-V_{Ti})^{3-}$ defect complex and guides the thermal processing condition for strong photocatalytic activity of Nb-doped anatase TiO_2.

Appendix A. Supplementary data

Supplementary data associated with this article can be found, in the online version, at http://dx.doi.org/10.1016/j.apcatb.2017.01.039.

References

[1] A. Fujishima, K. Honda, Electrochemical photolysis of water at a semiconductor electrode, Nature 238 (1972) 37–38.
[2] R. Asahi, T. Morikawa, T. Ohwaki, K. Aoki, Y. Taga, Visible-light photocatalysis in nitrogen-doped titanium oxides, Science 293 (2001) 269–271.
[3] M. Fujihira, Y. Satoh, T. Osa, Heterogeneous photocatalytic oxidation of aromatic compounds on TiO_2, Nature 293 (1981) 206–208.
[4] F. Fresno, R. Portela, S. Suárez, J.M. Coronado, Photocatalytic materials: recent achievements and near future trends, J. Mater. Chem. A 2 (2014) 2863–2883.
[5] J. Schneider, M. Matsuoka, M. Takeuchi, J. Zhang, Y. Horiuchi, M. Anpo, D.W. Bahnemann, Understanding TiO_2 photocatalysis: mechanisms and materials, Chem. Rev. 114 (2014) 9919–9986.
[6] Y. Kou, J. Yang, B. Li, S. Fu, Solar photocatalytic activities of porous Nb-doped TiO_2 microspheres by coupling with tungsten oxide, Mater. Res. Bull. 64 (2015) 105–111.
[7] K. Nakata, A. Fujishima, TiO_2 photocatalysis: design and applications, J. Photonchem. Photobiol. C: Photochem. Rev. 13 (2012) 169–189.
[8] C. Das, I. Paramasivam, N. Liu, P. Schmuki, Photoelectrochemical and photocatalytic activity of tungsten doped TiO_2 nanotube layers in the near visible region, Electrochim. Acta 56 (2011) 10557–10561.
[9] N. Feng, Q. Wang, A. Zheng, Z. Zhang, J. Fan, S.-B. Liu, J.-P. Amourex, F. Deng, Understanding the high photocatalytic activity of (B Ag)-codoped TiO_2 under solar-light irradiation with XPS, solid-state NMR, and DFT calculations, J. Am. Chem. Soc. 135 (2013) 1607–1616.
[10] H. Choi, D. Shin, B.C. Yeo, T. Song, S.S. Han, N. Park, S. Kim, Simultaneously controllable doping sites and the activity of a W-N co-doped TiO_2 photocatalyst, ACS Catal. 6 (2016) 2745–2753.
[11] Y. Shen, T. Xiong, T. Li, K. Yang, Tungsten and nitrogen Co-doped TiO_2 nano-powders with strong visible light response, Appl. Catal. B: Environ. 83 (2008) 177–185.
[12] A. Kubacka, G. Colón, M. Fernández-García, N- and/or W-(co)doped TiO_2-anatase catalysts: effect of the calcination treatment on photoactivity, Appl. Catal. B: Environ. 95 (2010) 238–244.
[13] A. Kubacka, A. Bachiller-Baeza, G. Colón, M. Fernández-García, Doping level effect on sunlight-driven W,N-co-doped TiO_2-anatase photo-catalysts for aromatic hydrocarbon partial oxidation, Appl. Catal. B: Environ. 93 (2010) 274–281.
[14] J.Z. Bloh, A. Folli, D. Macphee, Adjusting nitrogen doping level in titanium dioxide by codoping with tungsten: properties and band structure of the resulting materials, J. Phys. Chem. C 118 (2014) 21281–21292.

[15] M. Yang, D. Kim, H. Jha, K. Lee, J. Paul, P. Schmuki, Nb doping of TiO$_2$ nanotube for an enhanced efficiency of dye-sensitized solar cells, Chem. Commun. 47 (2011) 2032–2034.

[16] H. Su, Y.-T. Huang, Y.-H. Chang, P. Zhai, N.Y. Hau, P.C.H. Cheung, W.T. Yeh, T.C. Wei, S.P. Feng, The saynthesis of Nb-doped TiO$_2$ nanoparticles for improved-performance dye synthesized solar cells, Electrochim. Acta 182 (2015) 230–237.

[17] A.V. Emeline, Y. Furubayashi, X. Zhang, M. Jin, T. Murakami, A. Fujishima, Photoelectrochemical behavior of Nb-doped TiO$_2$ electrodes, J. Phys. Chem. B 109 (2005) 24441–24444.

[18] A.K. Chandiran, F. Sauvage, M. Casas-Cabanas, P. Comte, S.M. Zakeeruddin, M. Graetzel, Doping a TiO$_2$ photoanode with Nb^{5+} to enhance transparency and charge collection efficiency in dye- sensitized solar cells, J. Phys. Chem. B 114 (2010) 15849–15856.

[19] S.-L. Yang, J.-M. Wu, Effects of Nb$_2$O$_5$ in (Ba,Bi,Nb)-added TiO$_2$ ceramic varistors, J. Mater. Res. 10 (1995) 345–352.

[20] C. Das, P. Roy, M. Yang, H. Jha, P. Schmuki, Nb doped TiO$_2$ nanotubes for enhanced photoelectrochemical water-splitting, Nanoscale 3 (2011) 3094–3096.

[21] E. Uyanga, A. Gibaud, P. Daniel, D. Sangaa, G. Sevjidsuren, P. Altantsog, T. Beuvier, C.H. Lee, A.M. Balagurov, Structural and vibrational investigations of Nb-doped TiO$_2$ thin films, Mater. Res. Bull. 60 (2014) e222–e231.

[22] H. Choi, S.H. Cho, S. Khan, K.-R. Lee, S. Kim, Roles of an oxygen Frenkel pair in the photoluminescence of Bi^{3+}-doped Y$_2$O$_3$: Computational predictions and experimental verifications, J. Mater. Chem. C 2 (2014) 6017–6024.

[23] H. Choi, E.-K. Lee, S.B. Cho, D.S. Yoo, Y.-C. Chung, Interface-dependent spin-reorientation energy barrier in Fe/MgO thin film, IEEE Electron Device Lett. 32 (2011) 1287–1289.

[24] J. Ihm, A. Zunger, M.L. Cohen, Momentum-space formalism for the total energy of solids, J. Phys. C: Solid State Phys. 12 (1979) 4409–4422.

[25] W. Kohn, L.J. Sham, Self-consistent equations including exchange and correlation effects, Phys. Rev. 140 (1965) A1133–A1138.

[26] J.P. Perdew, K. Burke, M. Ernzerhof, Generalized gradient approximation made simple, Phys. Rev. Lett. 78 (1997) 3865–3868.

[27] J.P. Perdew, J.A. Chevary, S.H. Vosko, K.A. Jackson, M.R. Pederson, D.J. Singh, C. Fiolhais, Atoms, molecules, solids, and surfaces: applications of the generalized gradient approximation for exchange and correlation, Phys. Rev. B 46 (1992) 6671–6687.

[28] G. Kresse, J. Hafner, Ab initio molecular dynamics for liquid metals, Phys. Rev. B 47 (1993) 558–561.

[29] H.J. Monkhorst, J.D. Pack, Special points for Brillouin-zone integrations, Phys. Rev. B 13 (1976) 5188–5192.

[30] S.L. Dudarev, G.A. Botton, S.Y. Savrasov, C.J. Humphreys, A.P. Sutton, Electron-energy-loss spectra and the structural stability of nickel oxide: an LSDA + U study, Phys. Rev. B 57 (1998) 1505–1509.

[31] C. Freysoldt, B. Grabowski, T. Hickel, J. Neugebauer, G. Kresse, A. Janotti, C.G. Van de Walle, First-principles calculations for point defects in solids, Rev. Mod. Phys. 86 (2014) 253–305.

[32] C.G. Van de Walle, J. Neugebauer, First-principles calculations for defects and impurities: applications to III-nitrides, J. Appl. Phys. 95 (2004) 3851–3879.

[33] M. Harb, P. Sautet, P. Raybaud, Origin of the enhanced visible-light absorption in N-doped bulk anatase TiO$_2$ from First-principles calculations, J. Phys. Chem. C 115 (2011) 19394–19404.

[34] J. Heyd, G.E. Scuseria, M. Ernzerhof, Hybrid functionals based on a screened Coulomb potential, J. Chem. Phys. 118 (2004) 8207–8215.

[35] K. Reuter, M. Scheffler, Composition, structure, and stability of RuO$_2$(110) as a function of oxygen pressure, Phys. Rev. B 65 (2001) 035406.

[36] D. Kim, B.C. Yeo, D. Shin, H. Choi, S. Kim, N. Park, S.S. Han, Phys. Rev. B 95 (2017) 045209.

[37] Z.Q. Li, C.C. Wang, L.G. Fu, E.M. Li, H.H. Lin, Y.D. Song, Mesoporous TiO$_2$ yolk-shell microspheres for dye-sensitized solar cells with a high efficiency exceeding 11%, Sci. Rep. 5 (2015) 14178:1–14178:8.

[38] H. Kamisaka, T. Hitosugi, T. Suenaga, T. Hasegawa, K. Yamashita, Density functional theory based First-principles calculation of Nb-doped anatase TiO$_2$ and its interactions with oxygen vacancies and interstitial oxygen, J. Chem. Phys. 131 (2009) 034702:1–034702:10.

[39] T. Miyagi, M. Kamei, I. Sakaguchi, T. Mitsuhashi, A. Yamazaki, Photocatalytic property and deep levels of Nb-doped anatase TiO$_2$ film grown by metalorganic chemical vapor deposition, Jpn. J. Appl. Phys. 43 (2004) 775–776.

[40] M.C. Mathapa, A.K. Tripathi, M.K. Singh, S.P. Gairola, S.N. Pendey, A. Agarwal, Effect of annealing temperature and Raman spectra of TiO$_2$ particles, Chem. Phys. Lett. 555 (2013) 182–186.

[41] S.G. Kim, M.J. Ju, T.T. Choi, W.S. Choi, H.J. Choi, J.B. Baek, H.K. Kim, Nb-doped TiO$_2$ nanoparticles for organic dye-sensitized solar cells, RSC Adv. 3 (2013) 16380–16386.

[42] H.C. Choi, Y.M. Jung, S.B. Kim, Size effects in the Raman spectra of TiO$_2$ nanoparticles, Vib. Spectrosc. 37 (2005) 33–38.

[43] M. Pal, U. Pal, J.M.G.Y. Jimenez, F.P. Roddrigue, Effect of crystallization and dopant concentration on the emission behavior of TiO$_2$:Eu nanophosphor, Nanoscale Res. Lett. 7 (2012) 1–12.

[44] L. Kong, C. Wang, H. Zheng, X. Zhang, Y. Liu, Defect-induced yellow color in Nb-doped TiO$_2$ and its impact on visible-light photocatalysis, J. Phys. Chem. C 119 (2015) 16623–16632.